frontiers in Earth Science

ORIGINAL RESEARCH
published: 05 November 2020
doi: 10.3389/feart.2020.588310

Mechanisms of Pyrite Formation Promoted by Sulfate-Reducing Bacteria in Pure Culture

Arnaud Duverger[1,2]*, *Jasmine S. Berg*[1,3], *Vincent Busigny*[2,4], *François Guyot*[1,4], *Sylvain Bernard*[1] and *Jennyfer Miot*[1]

[1]Muséum National d'Histoire Naturelle, Sorbonne Université, CNRS UMR 7590, Institut de Minéralogie, de Physique des Matériaux et de Cosmochimie (IMPMC), Paris, France, [2]Université de Paris, Institut de physique du globe de Paris, CNRS, F-75005 Paris, France, [3]Department of Environmental Systems Science, Institute of Biogeochemistry and Pollutant Dynamics, Eidgenössische Technische Hochschule Zurich, Zurich, Switzerland, [4]Institut Universitaire de France, Paris, France

OPEN ACCESS

Edited by:
Guillaume Paris,
Centre de Recherches Pétrographiques et Géochimiques (CRPG), France

Reviewed by:
Alexey Kamyshny,
Ben-Gurion University of the Negev, Israel
Morgan Reed Raven,
University of California, Santa Barbara, United States

***Correspondence:**
Arnaud Duverger
arnaud.duverger@normalesup.org

Specialty section:
This article was submitted to Biogeoscience, a section of the journal Frontiers in Earth Science

Received: 28 July 2020
Accepted: 17 September 2020
Published: 05 November 2020

Citation:
Duverger A, Berg JS, Busigny V, Guyot F, Bernard S and Miot J (2020) Mechanisms of Pyrite Formation Promoted by Sulfate-Reducing Bacteria in Pure Culture. Front. Earth Sci. 8:588310. doi: 10.3389/feart.2020.588310

Pyrite, or iron disulfide, is the most common sulfide mineral on the Earth's surface and is widespread through the geological record. Because sulfides are mainly produced by sulfate-reducing bacteria (SRB) in modern sedimentary environments, microorganisms are assumed to drive the formation of iron sulfides, in particular, pyrite. However, the exact role played by microorganisms in pyrite formation remains unclear and, to date, the precipitation of pyrite in microbial cultures has only rarely been achieved. The present work relies on chemical monitoring, electron microscopy, X-ray diffraction, and synchrotron-based spectroscopy to evaluate the formation of iron sulfides by the sulfate-reducing bacteria *Desulfovibrio desulfuricans* as a function of the source of iron, either provided as dissolved Fe^{2+} or as Fe^{III}-phosphate nanoparticles. Dissolved ferrous iron led to the formation of increasingly crystalline mackinawite (FeS) with time, encrusting bacterial cell walls, hence preventing further sulfate reduction upon day 5 and any evolution of iron sulfides into more stable phases, e.g., pyrite. In contrast, ferric phosphate was transformed into a mixture of large flattened crystals of well-crystallized vivianite ($Fe_3(PO_4)_2 \cdot 8H_2O$) and a biofilm-like thin film of poorly crystallized mackinawite. Although being hosted in the iron sulfide biofilm, most cells were not encrusted. Excess sulfide delivered by the bacteria and oxidants (such as polysulfides) promoted the evolution of mackinawite into greigite (Fe_3S_4) and the nucleation of pyrite spherules. These spherules were several hundreds of nanometers wide and occurred within the extracellular polymeric substance (EPS) of the biofilm after only 1 month. Altogether, the present study demonstrates that the mineral assemblage induced by the metabolic activity of sulfate-reducing bacteria strongly depends on the source of iron, which has strong implications for the interpretation of the presence of pyrite and vivianite in natural environments.

Keywords: sulfate-reducing bacteria, biomineralization, iron sulfide (FeS), pyrite (FeS_2), vivianite, electron micoscopy, scanning transmission X-ray microscopy

1 INTRODUCTION

Iron is the fourth most abundant element on the Earth's surface, but due to modern oxic conditions, dissolved Fe^{2+} concentration in modern ocean is low (around 20 nM). Only in some modern ferruginous environments, analogous to ancient ocean, does dissolved ferrous iron concentration reach millimolar levels (Lake Pavin and Kabuno Bay (Busigny et al., 2014; Crowe et al. 2014; Llirós et al., 2015)). In addition, iron can precipitate in different minerals depending on environmental conditions. Iron oxides/oxyhydroxides such as ferrihydrite ($Fe_5O_8H \cdot 4H_2O$), goethite (α-FeOOH), lepidocrocite (γ-FeOOH), and hematite (α-Fe_2O_3) are prevalent in oxic systems (Cornell and Schwertmann, 2003), associated with iron phyllosilicates (clays) and sometimes with ferric phosphate nanoparticles (chemically close to strengite ($FePO_4 \cdot 2H_2O$) in eutrophic environment due to the high levels of phosphate (Cosmidis et al., 2014)). In contrast, in phosphate-rich anoxic environments, iron minerals are dominated by ferrous phosphate vivianite ($Fe_3(PO_4)_2 \cdot 8H_2O$), e.g., in lacustrine environments (Rothe et al., 2016). Eventually, anoxic euxinic settings are dominated by iron sulfide minerals such as pyrite (FeS_2), greigite (Fe_3S_4), or mackinawite (FeS).

Pyrite (FeS_2) is the most thermodynamically stable iron sulfide mineral in anoxic low-temperature conditions (Schoonen, 2004) and is ubiquitous in both modern environments and the sedimentary record (Rickard et al., 2017). Although surface sulfide minerals can have diverse origins, sedimentary processes predominate over magmatic, hydrothermal, and volcanic ones (Rickard et al., 2017). In modern environments, sulfide formation is mainly driven by the metabolism of sulfate-reducing microorganisms (SRM), which are prevalent in anoxic environments, e.g., marine sediments or water column of permanently stratified euxinic waters such as the Black Sea (Vetriani et al., 2003) or Lake Cadagno (Tonolla et al., 2004) or even in ferruginous environments such as Lake Pavin (Lehours et al., 2005; Berg et al., 2016; Berg et al., 2019). Understanding the mechanisms of a possible biogenic pyrite formation pathway is crucial as pyrites are used as paleoenvironmental proxies and might also be good candidates for the search of biosignatures of early life (Shen and Buick, 2004). Sedimentary sulfides are generally enriched in light sulfur isotopes, suggesting their microbial origin (Thode et al., 1953). In addition, sedimentary pyrites generally display a specific texture called framboids (Rust, 1935), for which biogenic origin was proposed based on morphological criteria (Love, 1957; Folk, 2005). However, many reports of pyrite framboids formed under strictly abiotic conditions undermined their possible use as biosignatures (Berner, 1969; Farrand, 1970; Butler and Rickard, 2000; Ohfuji and Rickard, 2005). Later studies of sedimentary framboids using scanning transmission X-ray microscopy (Maclean et al., 2008) or nano-SIMS (Wacey et al., 2015) and revealing the presence of organic matter associated with framboids revived the biogenic interpretation. Since experimental biomineralization of framboidal pyrites has never been obtained, their biologic origin remains unfounded. Ultimately, while pyrite formation has been well constrained in abiotic systems, thanks to a set of experimental syntheses (Rickard and Luther, 2007), pathways of pyrite formation upon SRM activities remain largely unexplored.

Laboratory experiments are essential to understand the role of SRM in pyrite formation. Several studies of sulfate-reducing bacteria enrichments reported the formation of mackinawite (FeS) and greigite (Fe_3S_4), both being potential precursors of pyrite (Fortin et al., 1994; Herbert et al., 1998; Watson et al., 2000; Gramp et al., 2009). Pyrites were obtained in some enrichments (Donald and Southam, 1999; Thiel et al., 2019; Berg et al., 2020), supporting the role of biology in sedimentary pyrite formation. However, due to the huge diversity of bacteria in these enrichments, especially iron- and sulfur-cycling bacteria (Lehours et al., 2009; Sitte et al., 2013; Zeng et al., 2018; Berg et al., 2019), deciphering the specific role of sulfate-reducing bacteria is tricky. Despite several attempts at iron sulfide biomineralization in pure sulfate-reducing bacteria cultures, mackinawite was observed almost exclusively (Ivarson and Hallberg, 1976; Neal et al., 2001; Williams et al., 2005; Ikogou et al., 2017; Stanley and Southam, 2018) and sometimes in association with greigite (Zhou et al., 2014; Picard et al., 2018). Pyrite formation in pure sulfate-reducing bacteria cultures was reported in only a single instance (Rickard, 1969b).

In the present contribution, the sulfate-reducing bacterium *Desulfovibrio desulfuricans* was cultured with either dissolved Fe^{2+} or amorphous Fe^{III}-phosphate nanoparticles to investigate the effect of the iron source on the nature of iron sulfides formed. Sulfate-reducing bacteria promoted pyrite formation in the medium supplied with amorphous Fe^{III}-phosphate, whereas with dissolved Fe^{2+}, only mackinawite occurred. These results allow understanding of the evolution and mechanisms of pyrite formation in pure sulfate-reducing bacteria culture and discuss implications for natural environments.

2 MATERIALS AND METHODS

2.1 Culture and Biomineralization Conditions

All solution-preparation methods and manipulations were performed in a Jacomex® glove box under Ar (Alphagaz 1, Air Liquide) free of O_2 (<5 ppm), and solutions were prepared with Milli-Q water deoxygenated by N_2 (Alphagaz 1, Air Liquide) bubbling at 80 °C for 45 min.

The sulfate-reducing bacterium *Desulfovibrio desulfuricans* DSM642 (DSMZ, Germany) (Beijerinck, 1895) was pre-cultured in an anoxic iron-free medium composed of 2.84 g L^{-1} Na_2SO_4, 0.20 g L^{-1} KH_2PO_4, 0.30 g L^{-1} NH_4Cl, 0.50 g L^{-1} KCl, 2.00 g L^{-1} $MgCl_2 \cdot 6H_2O$, 0.15 g L^{-1} $CaCl_2 \cdot 2H_2O$, 1 mL L^{-1} trace element solution (Widdel et al., 1983), 1 mL L^{-1} selenite-tungstate solution (Tschech and Pfennig, 1984), 10 mL L^{-1} vitamin solution (Wolin et al., 1963), and 20 mM sodium DL-lactate. The pH was buffered with 3.00 g L^{-1} MOPS ($C_7H_{15}NO_4S$) and adjusted to 7.2 with sodium hydroxide (NaOH). Bacteria were inoculated in the pre-culture medium at 1 % (v/v), in 100-mL vials sealed with butyl rubber stoppers, and stored in the dark at 30 °C without stirring.

Once cells achieved the logarithmic phase of growth (around 1 week), they were centrifuged at 7,000 g for 10 min, rinsed three times in Milli-Q water, and transferred into a biomineralization medium at 50 % (v/v), corresponding to a final cell concentration of approximately 5×10^7 cells mL-1. The biomineralization medium was prepared in the same way as pre-culture medium but contained only Na_2SO_4, trace element, selenite-tungstate, vitamins, sodium DL-lactate, and MOPS buffer. A volume of 75 mL of the inoculated biomineralization medium was put into 100 mL serum vials and supplied with iron either as dissolved Fe^{2+} (20 mM) or nanoparticulate Fe^{III}-phosphate (10 mM). Dissolved ferrous iron was added from a 1 M solution of $FeCl_2 \cdot 4H_2O$. Nanoparticulate ferric phosphate was synthesized by successive addition of 2.72 g L^{-1} KH_2PO_4 and 5.56 g L^{-1} $FeSO_4 \cdot 7H_2O$ in a 0.1 M Na-acetate buffer solution, of pH 4.6 (Mirvaux et al., 2016). Culture vials were sealed with butyl rubber stoppers and incubated in the dark at 30 °C without stirring for 8 months. Chemical monitoring was performed in the first month. All biomineralization experiments were performed in triplicate. Abiotic controls were prepared with the complete mineralization medium and iron source but no inoculum of bacteria.

2.2 Chemical Monitoring

Biomineralization experiments and abiotic controls were sampled periodically to monitor the chemical evolution of the liquid medium during biomineralization. Aliquots of 3 mL were collected from the 75-mL serum vials with syringes and needles in the glove box. Samples for total and dissolved (0.2 μm-filtered; Merck Millipore) iron were fixed with HCl to a final concentration of 0.5 M. Samples for total and dissolved sulfide were fixed with zinc acetate to a 0.5 M concentration. A separate filtered aliquot was stored in the dark at 4 °C for dissolved phosphate and/or organic acid analyses.

Ferrous iron was analyzed spectrophotometrically with the ferrozine method (Stookey, 1970). Total iron was quantified by both a modified ferrozine method (Viollier et al., 2000) and ICP-AES (Perkin Elmer Optima 3,000). Sulfide concentrations were determined spectrophotometrically using the methylene blue method (Cline, 1969). Sulfate analysis was performed by ion chromatography (Dionex DX-600 IC System). Dissolved phosphate was measured spectrophotometrically using Biomol® Green Reagent (Enzo Life Sciences). Organic acids were detected by high-performance liquid chromatography (HPLC) on a U3000 Thermo Scientific series using a Rezex organic acid column (250 × 4.6 mm, 8 μm) with 5 mM H_2SO_4 as eluent.

2.3 Mineralogical Characterization

At selected time points, around 10 mL of suspended matter was collected by centrifugation at 7,000 g for 10 min and rinsed three times with deoxygenated Milli-Q water, and subsamples were deposited on a Si(111) wafer for X-ray diffraction (XRD), on a 200-mesh Formvar carbon copper grid (Agar Scientific, United Kingdom) for transmission electron microscopy (TEM), and on a silicon nitride window (Norcada, Canada) for scanning transmission X-ray microscopy (STXM). Scanning electron microscopy (SEM) samples were prepared by filtering 10–100 μL of the culture through a polycarbonate GTTP 0.2 μm filter (Merck Millipore, Darmstadt, Germany) and then rinsing with 10 mL of deoxygenated Milli-Q water. All samples were dried in the glove box and stored under anoxic conditions until analysis.

2.3.1 X-Ray Diffraction

Silicon wafers were mounted in an airtight cell equipped with a Kapton window designed for X-ray diffraction analyses under anoxic conditions. Diffraction patterns were acquired from 5° to 95° with a 2θ step of 0.033°, at 40 kV and 40 mA with Co Kα radiation on a PANalytical X'Pert Pro MPD diffractometer equipped with an X'celerator® detector mounted in Bragg-Brentano configuration.

2.3.2 Electron Microscopy

For scanning electron microscopy analyses, filters were mounted onto pin stubs with an adhesive carbon tape and then carbon coated before analysis in a Zeiss Ultra 55 scanning electron microscope equipped with a field emission gun (FEG) and a Brucker EDS Quantax detector (Brucker Corporation, Houston, TX, USA). Images were preferentially acquired under low-voltage conditions at 3 kV and 3 mm working distance with either a high-performance annular detector (secondary electrons) or an annular detector with filter grids (backscattered electrons). Higher-voltage images were acquired at 15 kV and 7.5 mm working distance with an Everhart Thornley detector (secondary electrons) or an angle selective backscattered detector. Elemental characterizations were performed by energy dispersive X-ray spectrometry (EDS) at 15 kV and 7.5 mm working distance.

For transmission electron microscopy analyses, copper grids were observed under a JEOL 2100F transmission electron microscope equipped with a field emission gun (FEG) operating at 200 kV. Selected-area electron diffraction (SAED) patterns were acquired on areas of interest. Scanning transmission electron microscopy (STEM) was performed in the high-angle annular dark field (HAADF) mode and coupled to energy dispersive X-ray spectrometry (EDS) mapping.

2.3.3 Scanning Transmission X-Ray Microscopy

Scanning transmission X-ray microscopy analyses at the C K-edge and Fe $L_{2,3}$-edges were performed at the HERMES beamline at SOLEIL (Saint-Aubin, France) (Belkhou et al., 2015; Swaraj et al., 2017). Energy was calibrated by setting the well-resolved 3p Rydberg peak of gaseous CO_2 at 294.96 eV for the C K-edge and the major L_2-edge peak of hematite at 708.5 eV for the Fe $L_{2,3}$-edges. Recommended procedures for radiation-sensitive samples were followed (Wang et al., 2009). In essence, image mapstacks were recorded at 288.2 and 280 eV for C K-edge and, then, image mapstacks were obtained on the same area from 690 to 740 eV for Fe $L_{2,3}$-edges. Data were processed using aXis2000 software (Hitchcock, 2019) following procedures described in previous studies (Miot et al., 2009b; Miot et al., 2009a). Near-edge X-ray absorption fine structure (NEXAFS) spectra for Fe $L_{2,3}$-edges were normalized by the double arctan method (Bourdelle et al., 2013). Several iron minerals were synthesized following reported procedures to serve as reference model compounds for scanning transmission X-ray microscopy analyses of Fe $L_{2,3}$-edges, including pyrite (Wei and Osseo-Asare, 1997), greigite (Li et al., 2014), mackinawite (Donald and Southam, 1999), vivianite (Miot

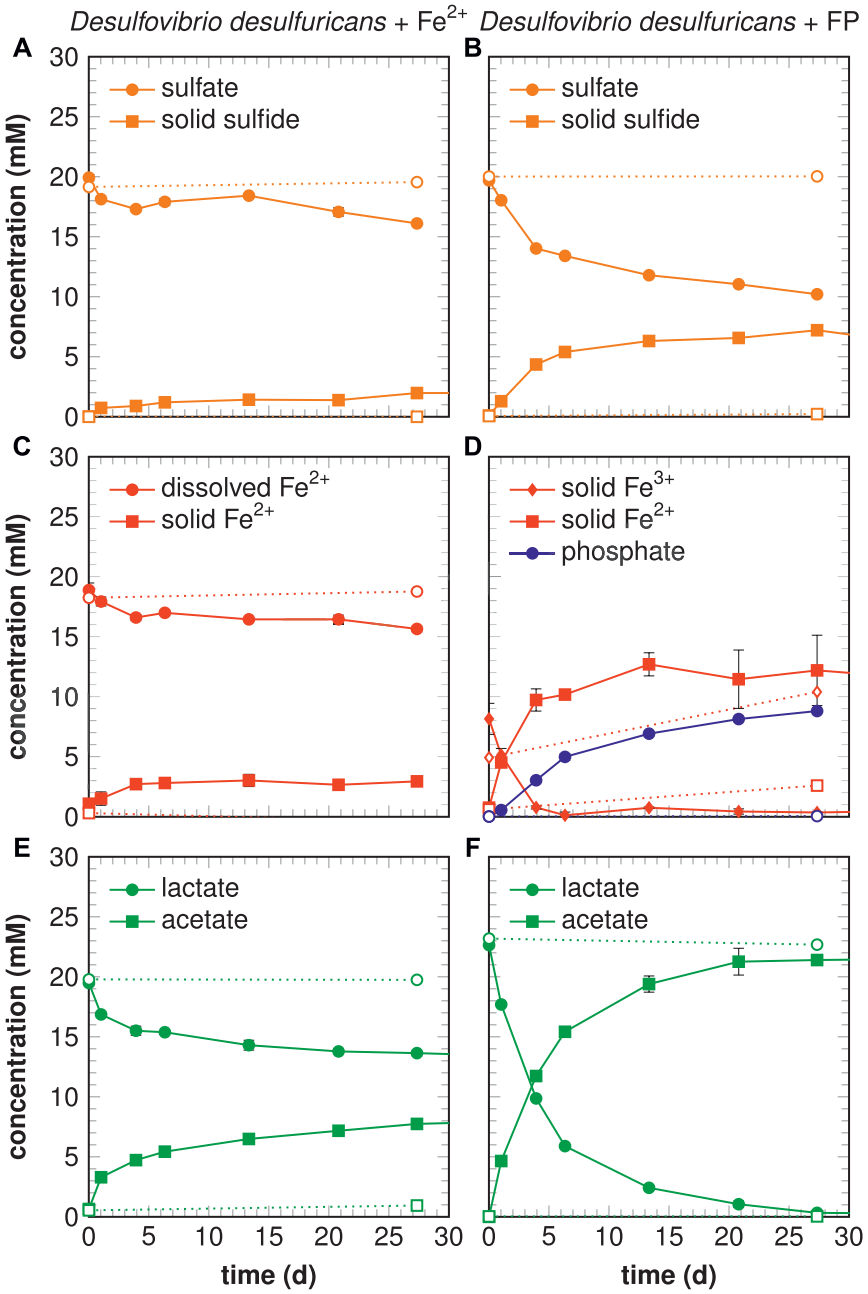

FIGURE 1 | Chemical compound concentrations in biotic (filled solid) and abiotic (open dotted) experiments for dissolved Fe^{2+} (left panels) and Fe^{III}-phosphate (right panels) conditions. **(A,B)** Sulfur compounds: dissolved sulfate (circle) and solid sulfide (square). **(C,D)** Iron and phosphate compounds: dissolved Fe^{2+} (circle), solid ferrous iron (square), solid ferric iron (diamond), and dissolved phosphate (circle). **(E,F)** Organic acid compounds: dissolved lactate (circle) and dissolved acetate (square).

et al., 2009a), amorphous ferric phosphate (Mirvaux et al., 2016), and hematite (Cornell and Schwertmann, 2003).

3 RESULTS

3.1 Chemical Evolution

Desulfovibrio desulfuricans was cultivated in two different biomineralization media containing 20 mM sulfate and 20 mM lactate, with initial iron provided either as 20 mM dissolved Fe^{2+} or 10 mM Fe in the form of nanoparticulate ferric phosphate, hereafter referred to as Fe-diss and FP-nano experiments, respectively. Dissimilatory sulfate reduction was attested in the two conditions by the formation of black precipitates of iron sulfides, whereas no precipitation was observed in abiotic controls. After 30 days of biomineralization, only 4 mM of sulfate was consumed in the Fe-diss condition (i.e., 20 % of initial sulfate

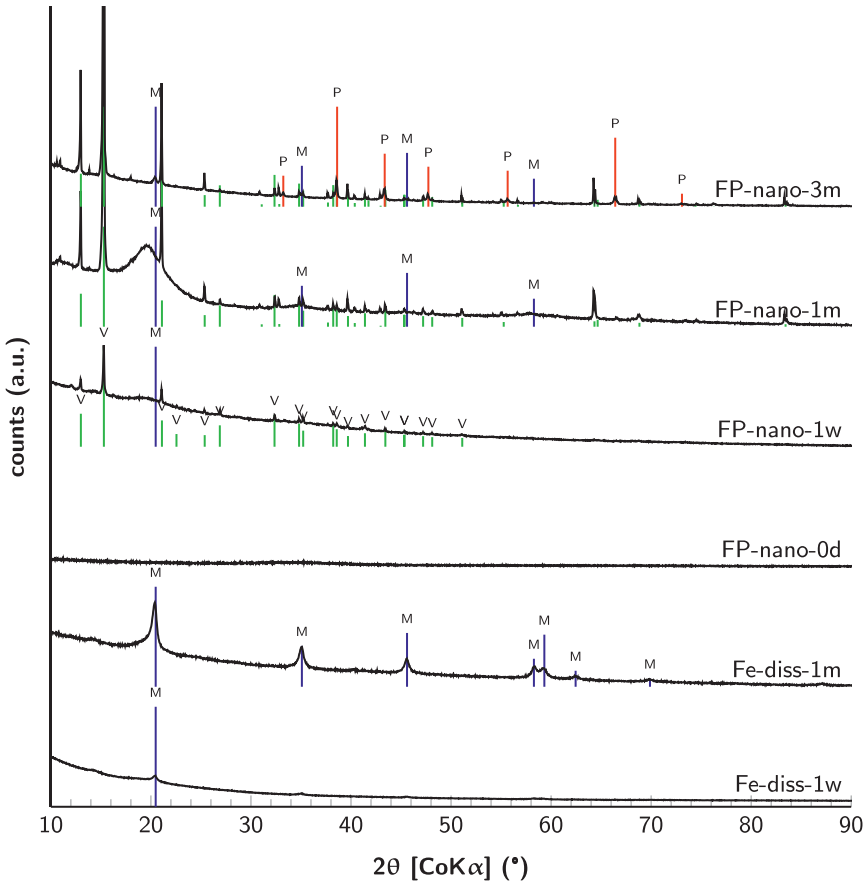

FIGURE 2 | X-ray diffractograms of solid phases in cultures after 1 week, 1 month, and 3 months as well as of initial nanoparticulate Fe^{III}-phosphate. Characteristic peaks of reference minerals are indexed for mackinawite (blue), vivianite (green), and pyrite (red).

concentration) (**Figure 1A**), while up to 10 mM was used in the FP-nano condition (i.e., half of initial sulfate) (**Figure 1B**). Simultaneously, 2 mM of solid sulfides (determined by the methylene blue method) were produced in the Fe-diss condition against 7 mM in the FP-nano condition, but no dissolved sulfide was detectable in both conditions (**Supplementary Table S1, S2**; **Figures 1A,B**). In contrast, no sulfate conversion was evidenced in the abiotic controls. After 1 month, 3 mM of Fe^{2+} was removed from the solution and precipitated as FeS in the Fe-diss condition (**Figure 1C**). In the FP-nano condition, solid Fe^{III} was rapidly reduced and precipitated as Fe-bearing minerals, so that dissolved iron trapped into or sorbed on minerals did not accumulate in the medium (**Supplementary Table S2**). This reduction-precipitation reaction was accompanied by the release of 9 mM dissolved phosphate in the FP-nano medium. Lactate was converted to acetate in both conditions, but in the Fe-diss condition, consumption of lactate (6 mM) was incomplete (**Figure 1E**), whereas all lactate was converted to acetate in the FP-nano condition (**Figure 1F**). No significant chemical changes were observed in abiotic controls for both conditions (**Figure 1**) with the exception of a slight increase in the Fe^{III} concentration. The apparent increase in solid Fe^{III} concentration is attributed to random sampling of suspended FP particles.

3.2 Mineralogical Characterization at the Bulk Scale

Solid phases were analyzed by X-ray diffraction (**Figure 2**). In the Fe-diss experiment, precipitates formed after 1 week of incubation were mostly amorphous with only a tiny peak at 20° 2θ angle (Co Kα), characteristic of mackinawite (FeS). After 1 month, mackinawite increased in crystallinity, as illustrated by several well-resolved peaks (Fe-diss-1m in **Figure 2**). In the FP-nano experiment, initial nanoparticulate Fe^{III}-phosphate was amorphous. After 1 week, vivianite ($Fe_3(PO_4)_2 \cdot 8H_2O$), as well as a poorly crystalline mackinawite phase, was detected, as suggested by the slight and broad band around 20° 2θ angle. Both phases gained in crystallinity after 1 month of incubation. Notably, pyrite (FeS_2), associated with mackinawite and vivianite, was detected after 3 months in the FP-nano condition.

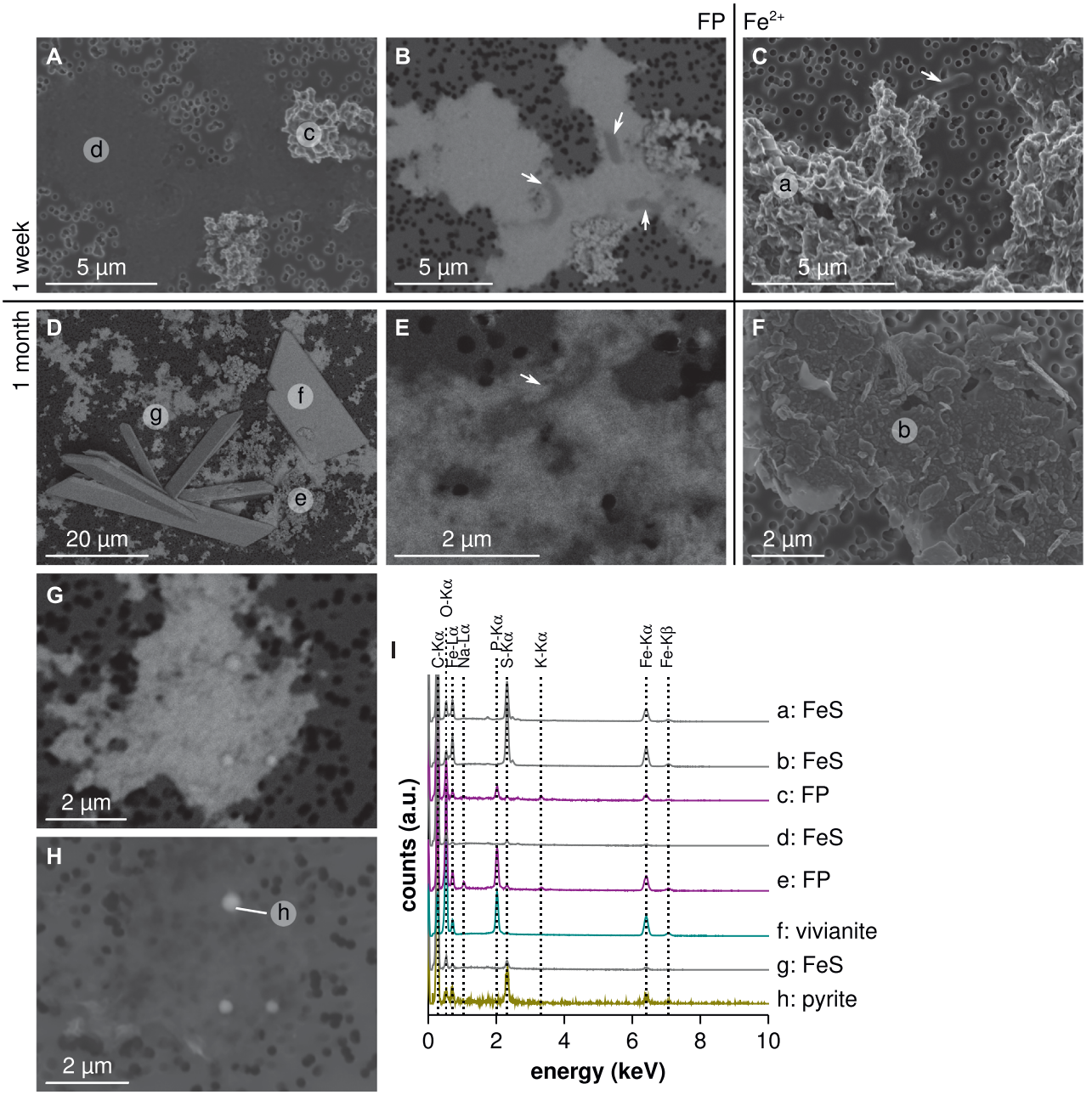

FIGURE 3 | SEM observations of precipitates obtained in both conditions, after 1 week and 1 month. **(A,B)** Comparison of secondary and backscattered electron images showing amorphous iron sulfide association with bacteria for FP-nano condition at 1 week. **(C)** Secondary electron images of Fe-diss condition at 1 week. **(D)** Large backscattered electron image at 1 month in FP-nano condition. **(E)** Backscattered electron image showing a bacterium within iron sulfide film at 1 month in FP-nano condition. **(F)** Secondary electron images of Fe-diss condition at 1 month. **(G,H)** Comparison of backscattered and secondary electron images showing pyrite spherules nucleating within the iron sulfide film at 1 month in FP-nano condition. **(I)** Energy dispersive X-ray spectrometry spectra pinned from previous SEM images. Letters in energy dispersive X-ray spectrometry maps correspond to energy dispersive X-ray spectrometry spectra provided in **(I)**. Except for **(H)**, all images were acquired in low-voltage conditions.

3.3 Microscopy Analyses of Mineral-Organic Assemblages

3.3.1 Fe-Diss Condition

Scanning electron microscopy and transmission electron microscopy observations of the products formed in the Fe-diss experiment revealed the presence of micrometer-scale aggregates of flake-like nanoparticles of iron sulfide at both 1 week and 1 month (**Figures 3C,F,I, 4A,D,E,H**). After 1 week, the presence of mackinawite was confirmed by the polycrystalline diffraction pattern (**Figure 4B**) and the high-

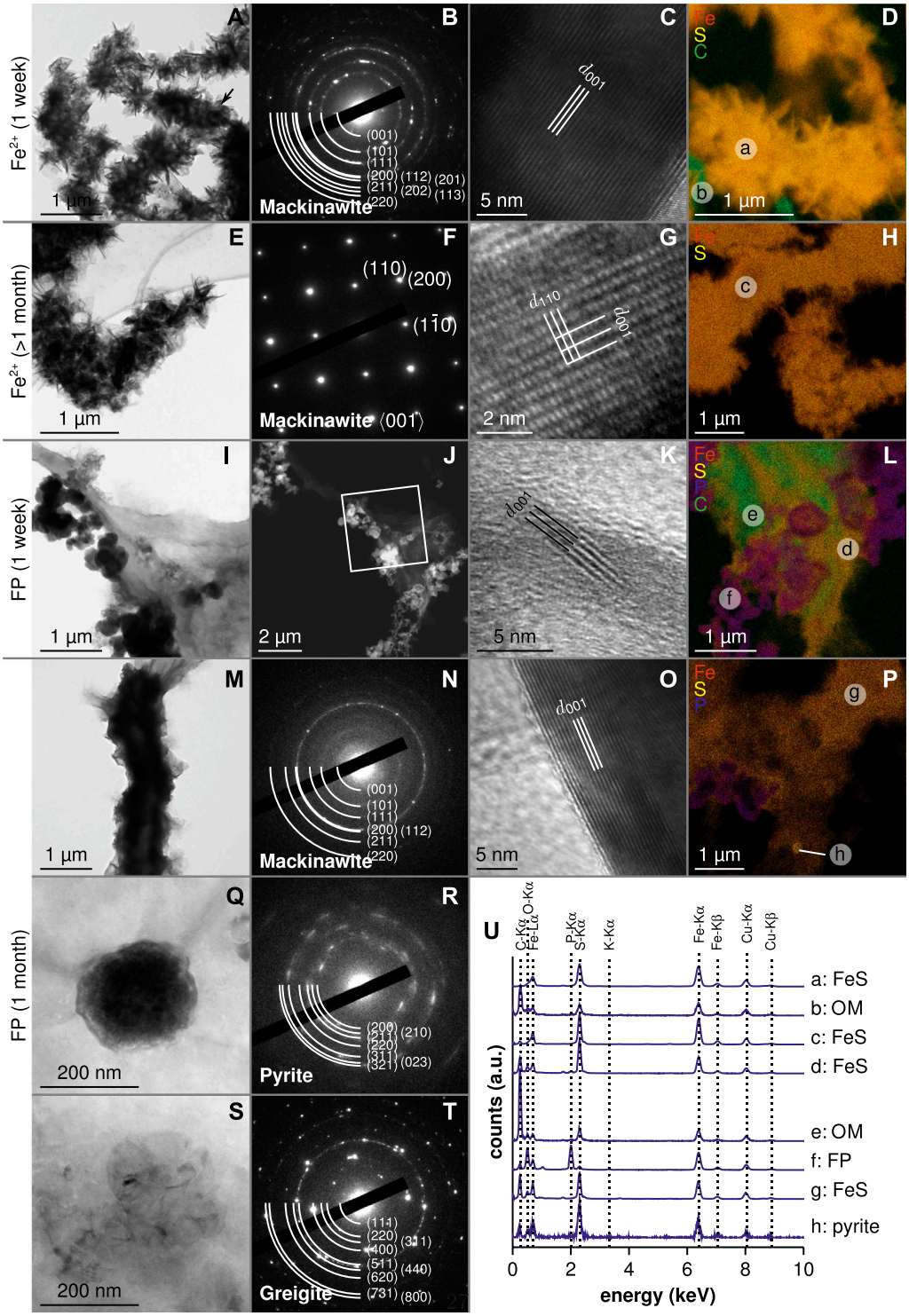

FIGURE 4 | Transmission electron microscopy observation of precipitates for both conditions, after 1 week and 1 month. Transmission electron microscopy, selected-area electron diffraction (or scanning transmission electron microscopy for **J** panel), high-resolution images and energy dispersive X-ray spectrometry map for: **(A–D)** Fe-diss condition at 1 week, **(E–H)** Fe-diss condition at 8 months, **(I–L)** FP-nano condition at 1 week, and **(M–T)** FP-nano condition at 1 month. **(U)** Energy dispersive X-ray spectrometry spectra pinned from previous energy dispersive X-ray spectrometry maps. Letters in energy dispersive X-ray spectrometry maps correspond to energy dispersive X-ray spectrometry spectra provided in **(U)**.

resolution images obtained by transmission electron microscopy, showing the 5 Å d-spacing characteristic of mackinawite (**Figure 4C**). Moreover, bacteria could be observed by scanning electron microscopy and transmission electron microscopy in association with mackinawite (**Figures 3C, 4A,D**). After 1 month, the increase in mackinawite crystallinity was confirmed by single-crystal diffraction patterns (**Figure 4F**). In these 1-month old samples, the size and shape of mackinawite aggregates suggested the presence of encrusted cells (**Figure 4E**).

3.3.2 FP-Nano Condition

Iron sulfides formed in the FP-nano experiment exhibited a morphology different from that obtained in the Fe-diss condition, specifically forming a thin film spreading over large areas (**Figures 3A,B,D,I, 4I,J,L,M,P,U**). After 1 week, this iron sulfide film was mostly amorphous, comprising only nano-domains of crystallized mackinawite (**Figure 4K**). Residual amorphous FP-nano was still present at both 1 week and 1 month (**Figures 3A,B,D,I, 4I,J,L,P,U, 5A,G**), but additional wide well-crystallized vivianite sheets (**Figures 3D,I**) were noticeable after 1 month. Due to mineral encrustation, bacteria could not be observed by scanning electron microscopy with secondary electrons (**Figure 3A**). However, scanning electron microscopy with backscattered electrons (**Figure 3B**), transmission electron microscopy (**Figure 4L**), and scanning transmission X-ray microscopy C K-edge analyses (**Figure 5B**) revealed that cells were intimately associated with the iron sulfide film. Scanning transmission X-ray microscopy analyses showed that this iron sulfide film had a structure close to that of mackinawite (**Figures 5C,G**). Mackinawite crystallinity increased from mostly amorphous after 1 week to large crystals (**Figure 4O**) attested by a polycrystalline mackinawite pattern (**Figure 4N**) after 1 month, similar to that observed in the Fe-diss condition after 1 week. Greigite domains of several hundreds of nanometers were also observed in the mackinawite film (**Figures 4S,T**). After 1 month, bacteria were still embedded within the mackinawite film (**Figures 3E, 4M,P, 5D,E,F,G**) and iron sulfide spherules of several hundreds of nanometers in size were observed within the iron sulfide film (**Figures 3G,H, 4Q**). These spherules had a higher S/Fe ratio than in mackinawite (**Figure 3I**, spot h). Transmission electron microscopy selected-area electron diffraction patterns indicated that they comprised pyrite particles nucleating within the FeS film (**Figure 4R**). The S/(Fe + S) ratio of these spherules was estimated to 66 % which is consistent with that of FeS_2 pyrite and significantly differs from the values, ranging from 45 to 55 % estimated for the iron sulfide film, consistent with FeS mackinawite. Scanning transmission X-ray microscopy data also confirmed the presence of pyrite, given the similarity of the spherules and reference pyrite spectra sharing a wider L_3-edge peak than the reference mackinawite spectrum and exhibiting a specific shoulder around 713.5 eV (**Figure 5G**).

4 DISCUSSION

4.1 First Stages of Iron Sulfide Formation (1 Week)

Although it is the most stable sulfide phase in sediments, pyrite is unlikely formed by the simple precipitation of Fe^{2+} and S_2^{2-} as the latter is not stable in low-temperature aqueous solutions (Kamyshny et al., 2004). Pyrite is the thermodynamically stable end product of multi-step pathways, some of which include metastable intermediates such as amorphous iron monosulfide, mackinawite, or greigite which are barely found in sediments (Berner, 1962; Pye, 1981). In aqueous low-temperature systems, mackinawite formation can be described as (Wei and Osseo-Asare, 1995)

$$Fe^{2+} + HS^- \rightarrow FeS + H^+ \quad (1)$$

This reaction is kinetically fast (Rickard, 1995), explaining the presence of amorphous iron sulfide (or disordered mackinawite) as the first product of abiotic pyrite synthesis in both ferrous and ferric-sulfide systems (Schoonen and Barnes, 1991; Wei and Osseo-Asare, 1997). Similarly, laboratory sulfate-reducing bacteria pure cultures have mainly yielded the formation of amorphous FeS (Fortin et al., 1994; Williams et al., 2005; Ntarlagiannis et al., 2005; Peltier et al., 2011; Stanley and Southam, 2018) or of well-crystallized mackinawite (Rickard, 1969b; Ivarson and Hallberg, 1976; Zhou et al., 2014; Ikogou et al., 2017; Picard et al., 2018). Some of these studies also detected greigite in long-term experiments (Rickard, 1969b; Picard et al., 2018) with excess of electron donor (Zhou et al., 2014).

In the two types of cultures performed in the present study, bacteria converted lactate and sulfate into acetate and sulfide, respectively, through sulfate respiration. Chemical monitoring (**Figures 1E,F**) showed a lactate/sulfate consumption ratio of ≈ two in agreement with sulfate respiration through incomplete oxidation of lactate (Muyzer and Stams, 2008):

$$2C_3H_5O_3^- + SO_4^{2-} \rightarrow 2CH_3COO^- + 2HCO_3^- + HS^- + H^+ \quad (2)$$

Hydrogen sulfide quickly reacted with the iron source to form and precipitate black iron sulfide preventing dissolved sulfide accumulation. After 1 week, iron sulfides were characterized as poorly crystallized mackinawite in both conditions (**Figure 2**). However, significant differences prevailed between Fe-diss and FP-nano experiments.

In Fe-diss condition, the flake-like morphology of iron sulfide aggregates (**Figures 3C, 4A**) was consistent with that in previous observations of iron sulfides formed in sulfate-reducing bacteria enrichments (Herbert et al., 1998; Watson et al., 2000; Sitte et al., 2013; Berg et al., 2019) or in pure cultures of sulfate-reducing bacteria (Picard et al., 2018; Stanley and Southam, 2018) in the presence of dissolved ferrous iron. In the present study, microbial activity has likely enhanced mackinawite crystallinity produced in one week as shown by the selected-area electron diffraction polycrystalline pattern (**Figure 4B**) and by high-resolution transmission electron microscopy that revealed large well-crystallized particles with typical (001) lattice fringes of mackinawite (**Figure 4C**). In contrast, abiotic precipitates were

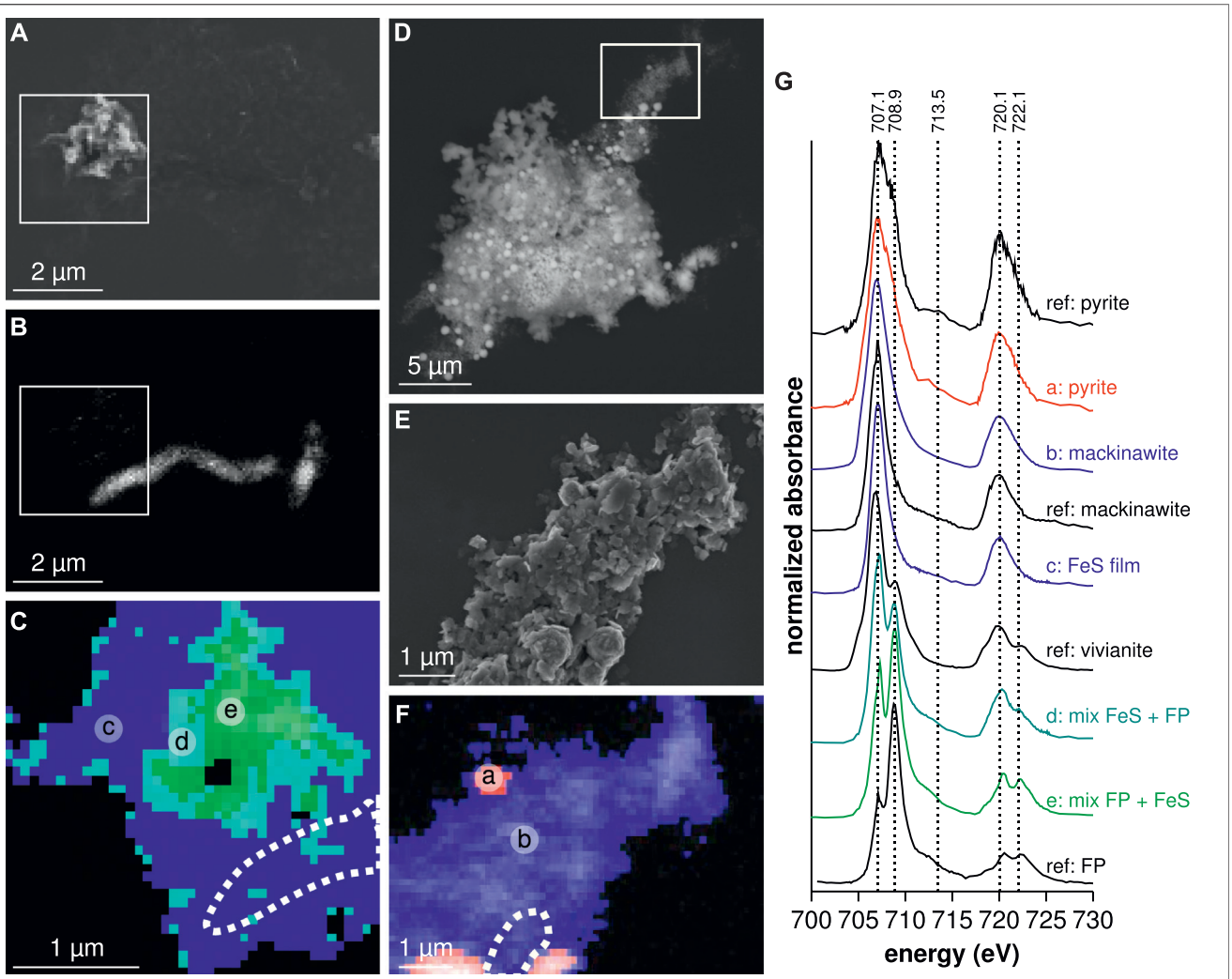

FIGURE 5 | SEM and STXM observations in FP-nano condition after 1 week and 6 months. **(A)** Secondary electron image at 1 week of bacteria embedded in the iron sulfide film close to an Fe^{III}-phosphate particle. **(B)** STXM C K-edge map of proteins obtained by subtracting the image at 270 eV from the image at 287 eV revealing bacteria from **(A)**. **(C)** STXM Fe $L_{2,3}$-edges composite map of the area squared in **(A,B)**. **(D)** Backscattered electron image at 6 months of multiple pyrite spherules within a mackinawite aggregate. **(E)** Secondary electron image of the area delineated in **(D)**. **(F)** Fe L-edges composite map of **(E)**. Dotted line showed bacteria revealed by scanning transmission X-ray microscopy C K-edge data. **(G)** Scanning transmission X-ray microscopy spectra pinned from previous composite maps. Letters in composite maps correspond to scanning transmission X-ray microscopy spectra provided in **(G)**.

usually reported as amorphous FeS (Ohfuji and Rickard, 2006; Csákberényi-Malasics et al., 2012; Picard et al., 2018). Transmission electron microscopy observations revealed that ≈ 10 µm-wide iron sulfide aggregates were in fact composed of elongated 1-µm long subunits, suggesting the presence of encrusted cells (**Figure 4A**). Cell wall surfaces are usually negatively charged and can thus offer binding sites for cations such as dissolved Fe^{2+}. In addition, the periplasm is also a dedicated site for Fe^{2+}-mineral precipitation as shown for iron-oxidizing bacteria (Miot et al., 2009c; Miot and Etique, 2016) and sulfate-reducing bacteria (Watson et al., 2000; Picard et al., 2018; Stanley and Southam, 2018). Sulfide released by sulfate-reducing bacteria would have promoted iron sulfide precipitation on the cell surface and/or within their periplasm, resulting in bacteria encrustation. Nonetheless, some studies reported thinner crusts (Fortin et al., 1994; Donald and Southam, 1999) to no encrustation (Stanley and Southam, 2018), questioning the mechanisms of cell encrustation in sulfate-reducing bacteria. As shown in Fe-oxidizing bacteria, cell wall encrustation can limit nutrient uptake eventually leading to cell death (Miot et al., 2015). Similarly, high sulfate-reducing bacteria encrustation levels in Fe-diss condition would explain the partial consumption of lactate and the strong slowdown of sulfate reduction after only 1 week (**Figures 1A,E**). In contrast to previous studies, these data show that encrustation apparently disturbs the metabolism of sulfate-reducing bacteria at least under millimolar dissolved Fe^{2+} concentrations (Watson et al., 2000; Picard et al., 2018). Such conditions differ from the low iron content of the modern ocean (nanomolar) or sediment porewater (hundreds of micromolars) but are expected in ferruginous

environments, e.g., in some meromictic lakes (Busigny et al., 2014; Llirós et al., 2015), where Fe-encrusted cells have been reported (Miot et al., 2016), as well as in extreme environments such as hydrothermal vents, acid mine drainage sites, and acid-sulfate systems in Yellowstone (Templeton, 2011). Encrustation patterns may vary across these environments depending on local Fe solubility.

While the mineralogy results of Fe-diss experiment after 1 week support previous findings reported in sulfate-reducing bacteria laboratory cultures, the biomineral products obtained in the FP-nano experiment after 1 week exhibit specific characteristics which were never described in previous studies. First of all, an iron sulfide thin film containing significant amounts of organic matter (**Figure 4L**) and hosting bacterial cells (**Figures 3B, 5B**) could be interpreted as a mineralized biofilm. Iron sulfide precipitation occurred in this thin layer rather than at the surface of iron phosphate nanoparticles, which were the source of this iron. This implies that HS produced by sulfate-reducing bacteria first reduced Fe^{III}-phosphate following the reaction

$$HS^- + H^+ + 2FePO_4 = S^0 + 2Fe^{2+} + 2HPO_4^{2-} \quad (3)$$

Coupling microbial sulfate-reduction (**Eq. 2**) and Fe^{III}-phosphate reduction (**Eq. 3**) allows one to explain that the 10 mM of Fe^{III} provided initially in the system was fully reduced by the consumption of 10 mM of lactate which is consistent with the results obtained on day 4 (**Figure 1B,F**). Dissolved Fe^{2+} released from Fe^{III}-phosphate reduction may be adsorbed on cell surfaces or onto extracellular polymeric substances (EPS) whose negative charges provide binding sites for cations (Ferris et al., 1987; Beveridge, 1989; Picard et al., 2018). Further HS^- produced by bacteria likely reacted with this adsorbed Fe^{2+} and precipitated as mackinawite according to **Eq. 1** to form an FeS film. In addition, dissolved Fe^{2+} and phosphate released by Fe^{III}-phosphate reduction (**Eq. 3**) precipitated as vivianite (**Figure 2**), due to its low solubility at the pH and temperature explored here (pKs $\approx$ 36 (Al-Borno and Tomson, 1994)), according to

$$2HPO_4^{2-} + 3Fe^{2+} + 8H_2O = Fe_3(PO_4)_2 \cdot 8H_2O + 2H^+. \quad (4)$$

The difference in mackinawite crystallinity in the two different biomineralization conditions could be explained by the local concentration of iron bound at the cell surface. In the Fe-diss condition, high amounts of Fe^{2+} were supplied in the starting biomineralization medium accounting for the significant precipitation of FeS in contact with the cell surface (**Figure 4A**). In contrast, Fe^{2+} in the FP-nano condition was gradually supplied by the reduction of Fe^{III}-phosphate leading to a lower concentration of cell-bound iron and thus a more diffuse precipitation of poorly crystalline mackinawite (**Figure 4K**) within a wide amorphous FeS film. Moreover, part of HS^- produced by sulfate-reducing bacteria was consumed by the reduction of ferric phosphate, thus decreasing its availability for iron sulfide precipitation and crystallization. This suggests that the consumption of sulfide through ferric iron reduction may delay the increase in mackinawite crystallinity. Phosphate might also be responsible for mackinawite's lack of crystallinity as it has been shown that adsorbed phosphate prevents the evolution of iron oxyhydroxides into well-crystallized phases (Borch et al., 2007; Voegelin et al., 2013; Schoepfer et al., 2019). Future studies aimed at evaluating the competition between phosphate and sulfide for reaction with ferrous iron would be of particular interest to disentangle the mechanisms at play.

4.2 Long-Term Iron Sulfide Evolution ($\geq$ 1 Month)

Aging of disordered mackinawite leads to its conversion into more stable iron sulfide phases such as crystalline mackinawite, greigite, or pyrite depending on environmental conditions. The increase in mackinawite crystallinity with aging has been interpreted as the expulsion of water molecules entrapped between lattice sheets during rapid mackinawite precipitation (Wolthers et al., 2003). In abiotic experiments, ordering of mackinawite is quite slow and could take several months to a year (Rickard, 1969a). In the present work, the high degree of mackinawite crystallinity in the Fe-diss condition is evidenced after only 1 month by X-ray diffraction (**Figure 2**), single-crystalline selected-area electron diffraction patterns obtained by transmission electron microscopy (**Figure 4F**), and high-resolution images (**Figure 4G**). Mackinawite increase in crystallinity was not as pronounced in the FP-nano experiment, but it showed relatively well-crystallized polycrystalline selected-area electron diffraction patterns after 1 month (**Figure 4N**), and the small nanometric domains present after 1 week (**Figure 4K**) evolved into domains of hundreds of nanometers long (**Figure 4O**). Interestingly, the morphology of mackinawite after 1 month in the FP-nano condition was similar to the one observed in the Fe-diss condition after 1 week.

In the absence of oxidants, the lack of other stable iron sulfides than well-crystallized mackinawite in the Fe-diss experiment could be explained by the low level of sulfide produced, around 2 mM, compared to the high dissolved Fe^{2+} concentration (over 15 mM, **Figure 1C**, **Supplementary Table S1**). In addition, both greigite and pyrite are more oxidized than mackinawite. However, iron and sulfur are as Fe^{2+} and S^{2-} in FeS mackinawite, two iron atoms out of three are Fe^{3+} in Fe_3S_4 greigite, and in pyrite, sulfur atoms are at the formal oxidation degree −1 in the disulfide ion S^{2-}. Oxidants are thus necessary for the conversion of mackinawite into pyrite. In aqueous solutions, protons might be the appropriate oxidants for the conversion of FeS into FeS_2 at low temperature as, for instance, in the H_2S pathway (Rickard, 1997; Rickard and Luther, 1997):

$$FeS + H_2S = FeS_2 + H_2 \quad (5)$$

The rate of **Eq. 5** has been well constrained (Rickard, 1997), and in Fe-diss condition, the formation of 1 mM pyrite after 1 month would require more than 1 mM of aqueous H_2S, which would have been detected with the Cline method, if present. As sulfide produced by sulfate-reducing bacteria first precipitates with dissolved Fe^{2+} to form FeS, the limited production of sulfide in the Fe-diss experiment may have hindered pyrite formation. This hypothesis is in agreement with thermodynamic models predicting a H_2S concentration of around 10 nM in the Fe-diss

condition which implies that thousands of years are needed to form 1 mM of pyrite (**Supplementary Table S3**). Although H_2 concentration was not measured, it would be interesting to investigate in future studies if the accumulation of H_2 could also have limited the formation of pyrite through this reaction (Thiel et al., 2019).

In the FP-nano experiment, the pyrite formation pathway assumed in the Fe-diss condition (**Eq. 5**) was shifted to a more efficient pathway involving zero-valent sulfur formed through the reduction of ferric phosphate (**Eq. 3**). Indeed, pyrite formation might be strongly accelerated if other oxidants than protons are available for oxidation of FeS into FeS_2. The only reported case where pyrite was indeed detected in pure sulfate-reducing bacteria cultures was in the presence of goethite (FeO(OH)) (Rickard, 1969b). In the present study, we report a second example of rapid pyrite formation in a pure culture of sulfate-reducing bacteria by using Fe^{III}-phosphate as an iron source. Thus, the presence of ferric iron (Fe^{III}-phosphate or goethite) in pure cultures appears to be a crucial parameter for the formation of pyrite. Reaction of sulfide with ferric iron described in **Eq. 3** likely provides zero-valent sulfur that can act as an oxidant promoting the conversion of mackinawite into pyrite as follows (Berner, 1970):

$$FeS + S^0 = FeS_2 \quad (6)$$

The occurrence of greigite within the iron sulfide film (**Figures 4S,T**) is consistent with the possible solid-state conversion of mackinawite into greigite (Lennie et al., 1997; Pósfai, 1998). Greigite may originate from the reaction of FeS with zero-valent sulfur:

$$3FeS + S^0 = Fe_3S_4 \quad (7)$$

Greigite possibly represents an intermediate phase in the global mechanism of pyrite formation, but it did not accumulate to sufficient levels to be detectable by X-ray diffraction analyses in the FP-nano condition. Pyrite formation through a greigite pathway has been suggested based on the occurrence of sedimentary magnetic pyrites and has been well studied (Wilkin and Barnes, 1996; Benning et al., 2000; Hunger and Benning, 2007; Lan and Butler, 2014). Although structurally complex (Rickard and Luther, 2007), the conversion of greigite to pyrite through a solid-state reaction may still be possible, as shown by hydrothermal experiments (Hunger and Benning, 2007) and, more recently, by the co-occurrence of greigite and nanocrystalline pyrite domains in micrometer-large pyrite spheres formed in an sulfate-reducing bacteria enrichment culture (Berg et al., 2020). Pyrite could thus have been produced by the reaction of greigite with zero-valent sulfur as follows:

$$Fe_3S_4 + 2S^0 = 3FeS_2 \quad (8)$$

Since FeS and S_0 (in the form of cyclo-octasulfur S_8) are both solid phases, a direct reaction between them in solution is improbable. Instead, S^0 may occur as polysulfides which have been shown to result from the reaction of HS^- with ferric phases, especially Fe^{III}-(hydr)oxides such as goethite or lepidocrocite (Hellige et al., 2012; Wan et al., 2014). In addition, polysulfides can be produced by the reaction of HS^- with elemental sulfur and exist in equilibrium depending on pH:

$$S^0_n + HS^- = S^{2-}_{n+1} + H^+ \quad (9)$$

Then, polysulfides may react with FeS to form pyrite as follows (Rickard, 1975):

$$FeS + Sn_{2-} = FeS_2 + S^{2-}_{n-1} \quad (10)$$

Interestingly, experiments with millimolar concentrations of dissolved Fe^{3+} did not yield pyrite formation even after almost a year (Ikogou et al., 2017). This suggests that the progressive supply of low amounts of dissolved Fe^{2+}, possibly by preventing cell encrustation and eventually cell death, is crucial. Low Fe^{2+} concentrations could be maintained by the presence of ferric minerals, organic-Fe^{3+} complexes, or low dissolved Fe^{3+} concentrations, rather than high concentrations of highly reactive dissolved Fe^{2+}. Such conditions are prevalent in many anoxic sedimentary environments and may thus best represent natural conditions of pyrite formation. Further experiments using more realistic (micromolar) concentrations of dissolved Fe^{2+} have to be conducted to evaluate the feasibility of biogenic pyrite formation in highly reduced environments. Moreover, the quantification of the evolution of Fe-bearing phases, for instance, by X-ray absorption spectroscopy, might help distinguish the types of iron sulfides in these biominerals over time.

4.3 Environmental Implications

Pyrite and vivianite are barely found together in natural environments and instead are usually reported to form separately (Manning et al., 1999). While pyrite is very abundant in anoxic sediments, in particular, in marine ones, due to the high level of sulfate in modern ocean, vivianite mainly forms in anoxic non-euxinic environments, such as some ferruginous meromictic lakes (Fagel et al., 2005; Rothe et al., 2014; Cosmidis et al., 2014). Indeed, highly reactive sulfide competes with phosphate for reaction with Fe^{2+}, hence preventing vivianite formation at high sulfide concentrations (Nriagu, 1972; Rothe et al., 2015). However, recent studies reported the formation of vivianite in euxinic environments in association with pyrite, e.g., in the Baltic Sea Fjords, the Black Sea, or Lake Cadagno, leading to sulfide depletion in sedimentary microenvironments or close to the water-sediment interface (Jilbert and Slomp, 2013; Dijkstra et al., 2014; Xiong et al., 2019). Here, we report the formation of both vivianite and pyrite in the presence of *D. desulfuricans*, starting from nanoparticulate Fe^{III}-phosphate, at high sulfate levels. These results confirm experimentally the possibility to form concomitantly vivianite and pyrite under euxinic conditions. Biogenic vivianite was often assumed to result from the activity of iron-reducing bacteria as it preferably forms in anoxic non-sulfidic environments rather than euxinic environments. However, enrichment cultures from the meromictic phosphate-rich Lake Pavin suggested that iron reduction and vivianite formation resulted from the activity of

both iron-reducing (*Pseudomonas* or *Clostridium*) and sulfate-reducing bacteria (Lehours et al., 2009; Berg et al., 2019). The results of the present study demonstrate that *Desulfovibrio desulfuricans* alone had the ability to induce vivianite formation in the FP-nano condition, suggesting that sulfate-reducing bacteria could play a significant role in vivianite formation in natural environments.

Despite a low sulfate concentration (<20 μM), Lake Pavin hosts a plethora of sulfate-reducing bacteria in its water column (Lehours et al., 2005; Berg et al., 2019; Berg et al., 2020) and pyrite was found abundantly in the first 12 cm of its sediments, in association with abundant vivianite (Viollier et al., 1997; Busigny et al., 2014; Busigny et al., 2016). Although pyrite was only detected in the sediments and not in the water column, sulfate-rich enrichment cultures from this lake led to rapid pyrite formation after 21 days of culture (Berg et al., 2020). Here, our results demonstrate that the sole activity of *Desulfovibrio* (representing 80 % of the microbial consortium in the enrichment (Berg et al., 2020)) was able to promote pyrite formation. However, while, in the present study, pyrites occurred as infra micrometric spherules undetectable by X-ray diffraction after one month, pyrites produced within the Lake Pavin consortium were visible on diffractograms after only 21 days and occurred as beads of 1 μm in diameter (Berg et al., 2020). The additional presence of sulfide-oxidizing bacteria (e.g., *Sulfuricurvum* and *Arcobacter*) might have strongly enhanced the rate of pyrite formation in the enrichment through an increased delivery of polysulfides (Berg et al., 2020). Hence, kinetics of pyrite formation induced by sulfate-reducing bacteria activity, such as described in our present study, would be accelerated under environmental conditions due to the concomitant activity of sulfide-oxidizing bacteria. In the future, it would be interesting to measure and compare the levels of polysulfides produced in pure sulfate-reducing bacteria vs mixed enrichment cultures in order to evaluate how S^0 impacts the formation of pyrite in both systems.

Sedimentary pyrites are commonly found as framboids of several micrometers in size (Wilkin et al., 1996; Busigny et al., 2016). Framboids are sparsely reported in anoxic water column and mainly in euxinic basins (Skei, 1988; Muramoto et al., 1991; Perry and Pedersen, 1993). Such framboids strongly deviate from the biogenic submicrometric pyrite spherules formed in the present FP-nano condition as well as from pyrites obtained in sulfate-reducing bacteria enrichments in previous studies (Donald and Southam, 1999; Thiel et al., 2019; Berg et al., 2020). This dichotomy suggests that framboids in natural environments originate from diagenetic processes rather than from purely biogenic pathways. We suggest that submicrometric pyrite spherules such as those obtained in our pure sulfate-reducing bacteria cultures (FP-nano condition) might be precursors for larger pyrite framboids. Framboidal evolution from biogenic precursors might explain the intra-grain δS^{34} variability in pyrite framboids (Bryant et al., 2020). In anoxic stratified waters, submicrometric pyrite spherules could form in the water column, below the oxycline, promoted by sulfate-reducing bacteria and other sulfur- and iron-cycling bacteria activities. Due to their small size and their dilution within the water column and the sediments, they may have been overlooked so far in euxinic and non-sulfidic water bodies. Interestingly, X-ray absorption spectroscopy analyses of Lake Pavin samples revealed that including pyrite significantly improved the fits of X-ray absorption spectroscopy spectra of samples collected just below the sulfate-reduction zone in this lake, while pyrites were not detected by X-ray diffraction (Cosmidis et al., 2014). Then, it is possible that pyrite precursors produced by sulfate-reducing bacteria in the water column would evolve into framboidal pyrites deeper in the sediments following diagenetic processes. This is consistent with the occurrence of pyrite microcrystals at the top of modern sediments which give way to pyrite framboids deeper in the sediment (Raven et al., 2016).

To conclude, our results attest that vivianite and pyrite formation can result from the single activity of sulfate-reducing bacteria in the presence of ferric phosphate nanoparticles. Early stages lead to the formation of submicrometric spherules nucleated within an FeS-rich film. Under environmental conditions, this reaction may be accelerated by the contribution of polysulfide-producing microorganisms. Evolution into micrometric framboidal pyrites may require longer timescales, hence occurring preferentially in the sediments upon diagenesis. Further investigations are needed to explore the effects of diagenesis on these pyrite spherules and understand the origin of pyrite framboids.

DATA AVAILABILITY STATEMENT

The raw data supporting the conclusions of this article will be made available by the authors, without undue reservation.

AUTHOR CONTRIBUTIONS

AD performed the laboratory experiments, AD, JSB, and JM achieved the chemical and mineralogical analyses. AD and FG realized the thermodynamic modeling. All the authors wrote and reviewed the manuscript.

ACKNOWLEDGMENTS

This work was funded by the ANR SRB project, under grant ANR-14-CE33-0003-01, of the French Agence Nationale de la Recherche to JM. The authors would like to thank the staff of the IMPMC (Sorbonne Universités) for their support and training on instruments: Benoît Baptiste and Ludovic Delbès for the X-ray diffraction facility, Jean-Michel Guigner for the transmission electron microscopy facility, Imène Estéve, Béatrice Doisneau, and Stéphanie Delbrel for the scanning electron microscopy facility, and Fériel Skouri-Panet and Mélanie Poinsot for the Biology Lab. The scanning electron microscopy facility at the IMPMC is funded by Région Ile de France, under grant SESAME 2006 N° I-07-593/R, INSU/CNRS, UPMC-Paris 6, and by the Agence Nationale de la Recherche (grant N° ANR-07-BLAN-

0124-01). The transmission electron microscopy facility at IMPMC is supported by Région Ile de France, under grant SESAME 2000 E 1435. Parts of this work were supported by IPGP multidisciplinary program PARI and by Paris-IdF region SESAME, under Grant no. 12015908. The authors thank Laure Cordier (LGE and IPGP) for ICP-AES and iron-chromatography analyses. The authors also thank Séverine Zirah (MCAM and MNHN) for providing access to high-performance liquid chromatography. The authors acknowledge SOLEIL (HERMES beamline, Saint-Aubin, France) for having provided beamtime for scanning transmission X-ray microscopy experiments. The authors also especially thank Sufal Swaraj, Stefan Stanescu, and Rachid Belkhou (SOLEIL) for their support at the beamlines.

SUPPLEMENTARY MATERIAL

The Supplementary Material for this article can be found online at: https://www.frontiersin.org/articles/10.3389/feart.2020.588310/full#supplementary-material.

REFERENCES

Al-Borno, A., and Tomson, M. B. (1994). The temperature dependence of the solubility product constant of vivianite. *Geochem. Cosmochim. Acta.* 58 (24), 5373–5378. doi:10.1016/0016-7037(94)90236-4

Beijerinck, M. (1895). Über Spirillum desulfuricans als ursache von sulfatreduktion. *Zentralbl. Bakteriol.* 1, 1–9.

Belkhou, R., Stanescu, S., Swaraj, S., Besson, A., Ledoux, M., Hajlaoui, M., et al. (2015). HERMES: a soft X-ray beamline dedicated to X-ray microscopy. *J. Synchrotron Radiat.* 22 (4), 968–979. doi:10.1107/s1600577515007778

Benning, L. G., Wilkin, R. T., and Barnes, H. L. (2000). Reaction pathways in the Fe–S system below 100°C. *Chem. Geol.* 167 (1-2), 25–51. doi:10.1016/s0009-2541(99)00198-9

Berg, J. S., Duverger, A., Cordier, L., Laberty-Robert, C., Guyot, F., and Miot, J. (2020). Rapid pyritization in the presence of a sulfur/sulfate-reducing bacterial consortium. *Sci. Rep.* 10 (1), 8264. doi:10.1038/s41598-020-64990-6

Berg, J. S., Jézéquel, D., Duverger, A., Lamy, D., Laberty-Robert, C., and Miot, J. (2019). Microbial diversity involved in iron and cryptic sulfur cycling in the ferruginous, low-sulfate waters of Lake Pavin. *PLoS One.* 14 (2), e0212787. doi:10.1371/journal.pone.0212787

Berg, J. S., Michellod, D., Pjevac, P., Martinez-Perez, C., Buckner, C. R. T., Hach, P. F., et al. (2016). Intensive cryptic microbial iron cycling in the low iron water column of the meromictic Lake Cadagno. *Environ. Microbiol.* 18 (12), 5288–5302. doi:10.1111/1462-2920.13587

Berner, R. A. (1970). Sedimentary pyrite formation. *Am. J. Sci.* 268 (1), 1–23. doi:10.2475/ajs.268.1.1

Berner, R. A. (1962). Tetragonal iron sulfide. *Science* 137 (3531), 669-669. doi:10.1126/science.137.3531.669-a

Berner, R. A. (1969). The synthesis of framboidal pyrite. *Econ. Geol.* 64 (4), 383–384. doi:10.2113/gsecongeo.64.4.383

Beveridge, T. J. (1989). Role of cellular design in bacterial metal accumulation and mineralization. *Annu. Rev. Microbiol.* 43 (1), 147–171. doi:10.1146/annurev.mi.43.100189.001051

Borch, T., Masue, Y., Kukkadapu, R. K., and Fendorf, S. (2007). Phosphate imposed limitations on biological reduction and alteration of ferrihydrite. *Environ. Sci. Technol.* 41 (1), 166–172. doi:10.1021/es060695p

Bourdelle, F., Benzerara, K., Beyssac, O., Cosmidis, J., Neuville, D. R., Brown, G. E., et al. (2013). Quantification of the ferric/ferrous iron ratio in silicates by scanning transmission X-ray microscopy at the Fe L2,3 edges. *Contrib. Mineral. Petrol.* 166 (2), 423–434. doi:10.1007/s00410-013-0883-4

Bryant, R. N., Jones, C., Raven, M. R., Owens, J. D., and Fike, D. A. (2020). Shifting modes of iron sulfidization at the onset of OAE-2 drive regional shifts in pyrite δ34S records. *Chem. Geol.* 553, 119808. doi:10.1016/j.chemgeo.2020.119808

Busigny, V., Jézéquel, D., Cosmidis, J., Viollier, E., Benzerara, K., Planavsky, N. J., et al. (2016). "The iron wheel in lac Pavin: interaction with phosphorus cycle," in *Lake Pavin*. Editors T. Sime-Ngando, P. Boivin, E. Chapron, D. Jezequel, and M. Meybeck (Cham: Springer International Publishing), 205–220.

Busigny, V., Planavsky, N. J., Jézéquel, D., Crowe, S., Louvat, P., Moureau, J., et al. (2014). Iron isotopes in an Archean ocean analogue. *Geochem. Cosmochim. Acta.* 133, 443–462. doi:10.1016/j.gca.2014.03.004

Butler, I. B., and Rickard, D. (2000). Framboidal pyrite formation via the oxidation of iron (II) monosulfide by hydrogen sulphide. *Geochem. Cosmochim. Acta.* 64 (15), 2665–2672. doi:10.1016/s0016-7037(00)00387-2

Cline, J. D. (1969). Spectrophotometric determination of hydrogen sulfide in natural waters[1]. *Limnol. Oceanogr.* 14 (3), 454–458. doi:10.4319/lo.1969.14.3.0454

Cornell, R. M., and Schwertmann, U. (2003). *The iron oxides: structure, properties, reactions, occurrences, and uses*. Weinheim: Wiley VCH. 2nd, completely rev. and extended ed edition.

Cosmidis, J., Benzerara, K., Morin, G., Busigny, V., Lebeau, O., Jézéquel, D., et al. (2014). Biomineralization of iron-phosphates in the water column of Lake Pavin (massif central, France). *Geochem. Cosmochim. Acta.* 126, 78–96. doi:10.1016/j.gca.2013.10.037

Csákberényi-Malasics, D., Rodriguez-Blanco, J. D., Kis, V. K., Rečnik, A., Benning, L. G., and Pósfai, M. (2012). Structural properties and transformations of precipitated FeS. *Chem. Geol.* 294-295, 249–258. doi:10.1016/j.chemgeo.2011.12.009

Dijkstra, N., Kraal, P., Kuypers, M. M. M., Schnetger, B., and Slomp, C. P. (2014). Are iron-phosphate minerals a sink for phosphorus in anoxic Black Sea sediments? *PLoS One.* 9 (7), e101139. doi:10.1371/journal.pone.0101139

Donald, R., and Southam, G. (1999). Low temperature anaerobic bacterial diagenesis of ferrous monosulfide to pyrite. *Geochem. Cosmochim. Acta.* 63 (13-14), 2019–2023. doi:10.1016/s0016-7037(99)00140-4

Fagel, N., Alleman, L., Granina, L., Hatert, F., Thamo-Bozso, E., Cloots, R., et al. (2005). Vivianite formation and distribution in Lake Baikal sediments. *Global Planet. Change.* 46 (1-4), 315–336. doi:10.1016/j.gloplacha.2004.09.022

Farrand, M. (1970). Framboidal sulphides precipitated synthetically. *Miner. Deposita.* 5 (3), 237–247. doi:10.1007/bf00201990

Ferris, F., Fyfe, W., and Beveridge, T. (1987). Bacteria as nucleation sites for authigenic minerals in a metal-contaminated lake sediment. *Chem. Geol.* 63 (3-4), 225–232. doi:10.1016/0009-2541(87)90165-3

Folk, R. L. (2005). Nannobacteria and the formation of framboidal pyrite: textural evidence. *J. Earth Syst. Sci.* 114 (3), 369–374. doi:10.1007/bf02702955

Fortin, D., Southam, G., and Beveridge, T. J. (1994). Nickel sulfide, iron-nickel sulfide and iron sulfide precipitation by a newly isolated Desulfotomaculum species and its relation to nickel resistance. *FEMS (Fed. Eur. Microbiol. Soc.) Microbiol. Ecol.* 14 (2), 121–132. doi:10.1111/j.1574-6941.1994.tb00099.x

Gramp, J. P., Wang, H., Bigham, J. M., Jones, F. S., and Tuovinen, O. H. (2009). Biogenic synthesis and reduction of Fe(III)-hydroxysulfates. *Geomicrobiol. J.* 26 (4), 275–280. doi:10.1080/01490450902892597

Hellige, K., Pollok, K., Larese-Casanova, P., Behrends, T., and Peiffer, S. (2012). Pathways of ferrous iron mineral formation upon sulfidation of lepidocrocite surfaces. *Geochem. Cosmochim. Acta.* 81, 69–81. doi:10.1016/j.gca.2011.12.014

Herbert, R. B., Benner, S. G., Pratt, A. R., and Blowes, D. W. (1998). Surface chemistry and morphology of poorly crystalline iron sulfides precipitated in media containing sulfate-reducing bacteria. *Chem. Geol.* 144 (1-2), 87–97. doi:10.1016/s0009-2541(97)00122-8

Hitchcock, A. P. (2019). aXis 2000–analysis of X-ray images and spectra.

Hunger, S., and Benning, L. G. (2007). Greigite: a true intermediate on the polysulfide pathway to pyrite. *Geochem. Trans.* 8, 1. doi:10.1186/1467-4866-8-1

Ikogou, M., Ona-Nguema, G., Juillot, F., Le Pape, P., Menguy, N., Richeux, N., et al. (2017). Long-term sequestration of nickel in mackinawite formed by Desulfovibrio capillatus upon Fe(III)-citrate reduction in the presence of thiosulfate. *Appl. Geochem.* 80, 143–154. doi:10.1016/j.apgeochem.2017.02.019

Ivarson, K. C., and Hallberg, R. O. (1976). Formation of mackinawite by the microbial reduction of jarosite and its application to tidal sediments. *Geoderma* 16 (1), 1–7. doi:10.1016/0016-7061(76)90089-6

Jilbert, T., and Slomp, C. P. (2013). Iron and manganese shuttles control the formation of authigenic phosphorus minerals in the euxinic basins of the Baltic Sea. *Geochem. Cosmochim. Acta.* 107, 155–169. doi:10.1016/j.gca.2013.01.005

Kamyshny, A., Goifman, A., Gun, J., Rizkov, D., and Lev, O. (2004). Equilibrium distribution of polysulfide ions in aqueous solutions at 25 °C: a new approach for the study of polysulfides' equilibria. *Environ. Sci. Technol.* 38 (24), 6633–6644. doi:10.1021/es049514e

Lan, Y., and Butler, E. C. (2014). Monitoring the transformation of mackinawite to greigite and pyrite on polymer supports. *Appl. Geochem.* 50, 1–6. doi:10.1016/j.apgeochem.2014.07.020

Lehours, A.-C., Bardot, C., Thenot, A., Debroas, D., and Fonty, G. (2005). Anaerobic microbial communities in Lake Pavin, a unique Meromictic Lake in France. *Aemilianense* 71 (11), 7389–7400. doi:10.1128/aem.71.11.7389-7400.2005

Lehours, A.-C., Batisson, I., Guedon, A., Mailhot, G., and Fonty, G. (2009). Diversity of culturable bacteria, from the anaerobic zone of the Meromictic Lake Pavin, able to perform dissimilatory-iron reduction in different *in Vitro* conditions. *Geomicrobiol. J.* 26 (3), 212–223. doi:10.1080/01490450902744012

Lennie, A. R., Redfern, S. A. T., Champness, P. E., Stoddart, C. P., Schofield, P. F., and Vaughan, D. J. (1997). Transformation of mackinawite to greigite; an *in situ* X-ray powder diffraction and transmission electron microscope study. *Am. Mineral.* 82 (3-4), 302–309. doi:10.2138/am-1997-3-408

Li, G., Zhang, B., Yu, F., Novakova, A. A., Krivenkov, M. S., Kiseleva, T. Y., et al. (2014). High-purity Fe3S4 greigite microcrystals for magnetic and electrochemical performance. *Chem. Mater.* 26 (20), 5821–5829. doi:10.1021/cm501493m

Llirós, M., García–Armisen, T., Darchambeau, F., Morana, C., Triadó–Margarit, X., Inceoğlu, O., et al. (2015). Pelagic photoferrotrophy and iron cycling in a modern ferruginous basin. *Sci. Rep.* 5 (1), 13803. doi:10.1038/srep13803

Love, L. G. (1957). Micro-organisms and the presence of syngenetic pyrite. *Quart. J. Geolog. Soc.* 113 (1-4), 429–440. doi:10.1144/gsl.jgs.1957.113.01-04.18

Maclean, L. C. W., Tyliszczak, T., Gilbert, P. U. P. A., Zhou, D., Pray, T. J., Onstott, T. C., et al. (2008). A high-resolution chemical and structural study of framboidal pyrite formed within a low-temperature bacterial biofilm. *Geobiology* 6 (5), 471–480. doi:10.1111/j.1472-4669.2008.00174.x

Manning, P. G., Prepas, E. E., and Serediak, M. S. (1999). Pyrite and vivianite intervals in the bottom sediments of eutrophic Baptiste Lake, Alberta, Canada. *Can. Mineral.* 37 (3), 593–601.

Miot, J., Benzerara, K., Morin, G., Bernard, S., Beyssac, O., Larquet, E., et al. (2009a). Transformation of vivianite by anaerobic nitrate-reducing iron-oxidizing bacteria. *Geobiology* 7 (3), 373–384. doi:10.1111/j.1472-4669.2009.00203.x

Miot, J., Benzerara, K., Morin, G., Kappler, A., Bernard, S., Obst, M., et al. (2009b). Iron biomineralization by anaerobic neutrophilic iron-oxidizing bacteria. *Geochem. Cosmochim. Acta.* 73 (3), 696–711. doi:10.1016/j.gca.2008.10.033

Miot, J., Benzerara, K., Obst, M., Kappler, A., Hegler, F., Schädler, S., et al. (2009c). Extracellular iron biomineralization by photoautotrophic iron-oxidizing bacteria. *Appl. Environ. Microbiol.* 75 (17), 5586–5591. doi:10.1128/aem.00490-09

Miot, J., and Etique, M. (2016). "Formation and transformation of iron-bearing minerals by iron(II)-oxidizing and iron(III)-reducing bacteria," in *Iron oxides*. Editor D. Faivre, (Weinheim, Germany: Wiley-VCH Verlag GmbH & Co. KGaA), 53–98.

Miot, J., Jézéquel, D., Benzerara, K., Cordier, L., Rivas-Lamelo, S., Skouri-Panet, F., et al. (2016). Mineralogical diversity in Lake Pavin: connections with water column chemistry and biomineralization processes. *Minerals*, 6 (2), 24. doi:10.3390/min6020024

Miot, J., Remusat, L., Duprat, E., Gonzalez, A., Pont, S., and Poinsot, M. (2015). Fe biomineralization mirrors individual metabolic activity in a nitrate-dependent Fe(II)-oxidizer. *Front. Microbiol.* 6, 879. doi:10.3389/fmicb.2015.00879

Mirvaux, B., Recham, N., Miot, J., Courty, M., Bernard, S., Beyssac, O., et al. (2016). Iron phosphate/bacteria composites as precursors for textured electrode materials with enhanced electrochemical properties. *J. Electrochem. Soc.* 163 (10), A2139–A2148. doi:10.1149/2.0101610jes

Muramoto, J. A., Honjo, S., Fry, B., Hay, B. J., Howarth, R. W., and Cisne, J. L. (1991). Sulfur, iron and organic carbon fluxes in the Black Sea: sulfur isotopic evidence for origin of sulfur fluxes. *Deep Sea Res. A.* 38, S1151–S1187. doi:10.1016/s0198-0149(10)80029-9

Muyzer, G., and Stams, A. J. M. (2008). The ecology and biotechnology of sulphate-reducing bacteria. *Nat. Rev. Microbiol.* 6, 441–454. doi:10.1038/nrmicro1892

Neal, A. L., Techkarnjanaruk, S., Dohnalkova, A., McCready, D., Peyton, B. M., and Geesey, G. G. (2001). Iron sulfides and sulfur species produced at hematite surfaces in the presence of sulfate-reducing bacteria. *Geochem. Cosmochim. Acta.* 65 (2), 223–235. doi:10.1016/s0016-7037(00)00537-8

Nriagu, J. O. (1972). Stability of vivianite and ion-pair formation in the system fe3(PO4)2-H3PO4H3PO4-H2o. *Geochem. Cosmochim. Acta.* 36 (4), 459–470. doi:10.1016/0016-7037(72)90035-x

Ntarlagiannis, D., Williams, K. H., Slater, L., and Hubbard, S. (2005). Low-frequency electrical response to microbial induced sulfide precipitation: electrical response to biominerals. *J. Geophys. Res.* 110 (G2). doi:10.1029/2005jg000024

Ohfuji, H., and Rickard, D. (2005). Experimental syntheses of framboids–a review. *Earth Sci. Rev.* 71 (3-4), 147–170. doi:10.1016/j.earscirev.2005.02.001

Ohfuji, H., and Rickard, D. (2006). High resolution transmission electron microscopic study of synthetic nanocrystalline mackinawite. *Earth Planet Sci. Lett.* 241 (1-2), 227–233. doi:10.1016/j.epsl.2005.10.006

Peltier, E., Ilipilla, P., and Fowle, D. (2011). Structure and reactivity of zinc sulfide precipitates formed in the presence of sulfate-reducing bacteria. *Appl. Geochem.* 26 (9-10), 1673–1680. doi:10.1016/j.apgeochem.2011.04.024

Perry, K. A., and Pedersen, T. F. (1993). Sulphur speciation and pyrite formation in meromictic ex-fjords. *Geochem. Cosmochim. Acta.* 57 (18), 4405–4418. doi:10.1016/0016-7037(93)90491-e

Picard, A., Gartman, A., Clarke, D. R., and Girguis, P. R. (2018). Sulfate-reducing bacteria influence the nucleation and growth of mackinawite and greigite. *Geochem. Cosmochim. Acta.* 220, 367–384. doi:10.1016/j.gca.2017.10.006

Pósfai, M. (1998). Reaction sequence of iron sulfide minerals in bacteria and their use as biomarkers. *Science* 280 (5365), 880–883.

Pye, K. (1981). Marshrock formed by iron sulphide and siderite cementation in saltmarsh sediments. *Nature* 294 (5842), 650–652. doi:10.1038/294650a0

Raven, M. R., Sessions, A. L., Fischer, W. W., and Adkins, J. F. (2016). Sedimentary pyrite δ34S differs from porewater sulfide in Santa Barbara Basin: proposed role of organic sulfur. *Geochem. Cosmochim. Acta.* 186, 120–134. doi:10.1016/j.gca.2016.04.037

Rickard, D. (1969a). The chemistry of iron sulphide formation at low temperatures. *Stock. Contrib. Geol.* 20, 67–95.

Rickard, D. (1969b). The microbiological formation of iron sulphides. *Stock. Contrib. Geol.*, 20:49–66.

Rickard, D. T. (1975). Kinetics and mechanism of pyrite formation at low temperatures. *Am. J. Sci.* 275 (6), 636–652. doi:10.2475/ajs.275.6.636

Rickard, D. (1995). Kinetics of FeS precipitation: Part 1. Competing reaction mechanisms. *Geochem. Cosmochim. Acta.* 59 (21), 4367–4379. doi:10.1016/0016-7037(95)00251-t

Rickard, D. (1997). Kinetics of pyrite formation by the H2S oxidation of iron (II) monosulfide in aqueous solutions between 25 and 125°C: the rate equation. *Geochem. Cosmochim. Acta.* 61 (1), 115–134. doi:10.1016/s0016-7037(96)00321-3

Rickard, D., and Luther, G. W. (1997). Kinetics of pyrite formation by the H2S oxidation of iron (II) monosulfide in aqueous solutions between 25 and 125°C: the mechanism. *Geochem. Cosmochim. Acta.* 61 (1), 135–147. doi:10.1016/s0016-7037(96)00322-5

Rickard, D., and Luther, G. W. (2007). Chemistry of iron sulfides. *Chem. Rev.* 107 (2), 514–562. doi:10.1021/cr0503658

Rickard, D., Mussmann, M., and Steadman, J. A. (2017). Sedimentary sulfides. *Elements* 13 (2), 117–122. doi:10.2113/gselements.13.2.117

Rothe, M., Frederichs, T., Eder, M., Kleeberg, A., and Hupfer, M. (2014). Evidence for vivianite formation and its contribution to long-term phosphorus retention in a recent lake sediment: a novel analytical approach. *Biogeosciences* 11 (18), 5169–5180. doi:10.5194/bg-11-5169-2014

Rothe, M., Kleeberg, A., Grüneberg, B., Friese, K., Pérez-Mayo, M., and Hupfer, M. (2015). Sedimentary sulphur:iron ratio indicates vivianite occurrence: a study from two contrasting freshwater systems. *PLoS One.* 10 (11), e0143737. doi:10.1371/journal.pone.0143737

Rothe, M., Kleeberg, A., and Hupfer, M. (2016). The occurrence, identification and environmental relevance of vivianite in waterlogged soils and aquatic sediments. *Earth Sci. Rev.* 158, 51–64. doi:10.1016/j.earscirev.2016.04.008

Rust, G. W. (1935). Colloidal primary copper ores at cornwall mines, southeastern Missouri. *J. Geol.* 43 (4), 398–426. doi:10.1086/624318

Schoepfer, V. A., Burton, E. D., and Johnston, S. G. (2019). Contrasting effects of phosphate on the rapid transformation of schwertmannite to Fe(III) (oxy)hydroxides at near-neutral pH. *Geoderma* 340, 115–123. doi:10.1016/j.geoderma.2018.12.051

Schoonen, M. A. A., and Barnes, H. L. (1991). Reactions forming pyrite and marcasite from solution: I. Nucleation of FeS2 below 100°C. *Geochem. Cosmochim. Acta.* 55 (6), 1495–1504. doi:10.1016/0016-7037(91)90122-l

Schoonen, M. A. (2004). "Mechanisms of sedimentary pyrite formation," in *Sulfur biogeochemistry - past and present* Editors J. P. Amend, K. J. Edwards, and T. W. Lyons. Geological Society of America, 117–134. doi:10.1130/0-8137-2379-5.117

Shen, Y., and Buick, R. (2004). The antiquity of microbial sulfate reduction. *Earth Sci. Rev.* 64 (3-4), 243–272. doi:10.1016/s0012-8252(03)00054-0

Sitte, J., Pollok, K., Langenhorst, F., and Küsel, K. (2013). Nanocrystalline nickel and cobalt sulfides formed by a heavy metal-tolerant, sulfate-reducing enrichment culture. *Geomicrobiol. J.* 30 (1), 36–47. doi:10.1080/01490451.2011.653082

Skei, J. (1988). Formation of framboidal iron sulfide in the water of a permanently anoxic fjord-framvaren, South Norway. *Mar. Chem.* 23 (3-4), 345–352. doi:10.1016/0304-4203(88)90103-x

Stanley, W., and Southam, G. (2018). The effect of gram-positive (Desulfosporosinus orientis) and gram-negative (Desulfovibrio desulfuricans) sulfate-reducing bacteria on iron sulfide mineral precipitation. *Can. J. Microbiol.* 64 (9), 629–637. doi:10.1139/cjm-2017-0545

Stookey, L. L. (1970). Ferrozine—a new spectrophotometric reagent for iron. *Anal. Chem.* 42 (7), 779–781. doi:10.1021/ac60289a016

Swaraj, S., Belkhou, R., Stanescu, S., Rioult, M., Besson, A., and Hitchcock, A. P. (2017). Performance of the HERMES beamline at the carbon K-edge. *J. Phys. Conf.* 849, 012046. doi:10.1088/1742-6596/849/1/012046

Templeton, A. S. (2011). Geomicrobiology of iron in extreme environments. *Elements* 7 (2), 95–100. doi:10.2113/gselements.7.2.95

Thiel, J., Byrne, J. M., Kappler, A., Schink, B., and Pester, M. (2019). Pyrite formation from FeS and H_2S is mediated through microbial redox activity. *Proc. Natl. Acad. Sci. U.S.A.* 116 (14), 6897–6902. doi:10.1073/pnas.1814412116

Thode, H. G., Macnamara, J., and Fleming, W. H. (1953). Sulphur isotope fractionation in nature and geological and biological time scales. *Geochem. Cosmochim. Acta.* 3 (5), 235–243. doi:10.1016/0016-7037(53)90042-8

Tonolla, M., Peduzzi, S., Demarta, A., Peduzzi, R., and Hahn, D. (2004). Phototropic sulfur and sulfate-reducing bacteria in the chemocline of meromictic Lake Cadagno, Switzerland. *J. Limnol.* 63 (2), 161–170. doi:10.4081/jlimnol.2004.161

Tschech, A., and Pfennig, N. (1984). Growth yield increase linked to caffeate reduction in Acetobacterium woodii. *Arch. Microbiol.* 137 (2), 163–167. doi:10.1007/bf00414460

Vetriani, C., Tran, H. V., and Kerkhof, L. J. (2003). Fingerprinting microbial assemblages from the oxic/anoxic chemocline of the Black Sea. *Appl. Environ. Microbiol.* 69 (11), 6481–6488. doi:10.1128/aem.69.11.6481-6488.2003

Viollier, E., Michard, G., Jézéquel, D., Pèpe, M., and Sarazin, G. (1997). Geochemical study of a crater lake: lake Pavin, Puy de Dôme, France. Constraints afforded by the particulate matter distribution in the element cycling within the lake. *Chem. Geol.*, 142(3-4):225–241. doi:10.1016/s0009-2541(97)00093-4

Viollier, E., Inglett, P. W., Hunter, K., Roychoudhury, A. N., and Van Cappellen, P. (2000). The ferrozine method revisited: Fe(II)/Fe(III) determination in natural waters. *Appl. Geochem.* 15 (6), 785–790. doi:10.1016/s0883-2927(99)00097-9

Voegelin, A., Senn, A.-C., Kaegi, R., Hug, S. J., and Mangold, S. (2013). Dynamic Fe-precipitate formation induced by Fe(II) oxidation in aerated phosphate-containing water. *Geochem. Cosmochim. Acta.* 117, 216–231. doi:10.1016/j.gca.2013.04.022

Wacey, D., Kilburn, M. R., Saunders, M., Cliff, J. B., Kong, C., Liu, A. G., et al. (2015). Uncovering framboidal pyrite biogenicity using nano-scale CNorg mapping. *Geology* 43 (1), 27–30. doi:10.1130/g36048.1

Wan, M., Shchukarev, A., Lohmayer, R., Planer-Friedrich, B., and Peiffer, S. (2014). Occurrence of surface polysulfides during the interaction between ferric (Hydr) Oxides and aqueous sulfide. *Environ. Sci. Technol.* 48 (9), 5076–5084. doi:10.1021/es405612f

Wang, J., Morin, C., Li, L., Hitchcock, A., Scholl, A., and Doran, A. (2009). Radiation damage in soft X-ray microscopy. *J. Electron. Spectrosc. Relat. Phenom.* 170 (1-3), 25–36. doi:10.1016/j.elspec.2008.01.002

Watson, J., Cressey, B., Roberts, A., Ellwood, D., Charnock, J., and Soper, A. (2000). Structural and magnetic studies on heavy-metal-adsorbing iron sulphide nanoparticles produced by sulphate-reducing bacteria. *J. Magn. Magn Mater.* 214 (1-2), 13–30. doi:10.1016/s0304-8853(00)00025-1

Wei, D., and Osseo-Asare, K. (1995). formation of iron monosulfide: a spectrophotometric study of the reaction between ferrous and sulfide ions in aqueous solutions. *J. Colloid Interface Sci.*, 174(2):273–282. doi:10.1006/jcis.1995.1392

Wei, D., and Osseo-Asare, K. (1997). Aqueous synthesis of finely divided pyrite particles. *Colloid. Surface. Physicochem. Eng. Aspect.* 121 (1), 27–36. doi:10.1016/s0927-7757(95)03502-8

Widdel, F., Kohring, G.-W., and Mayer, F. (1983). Tudies on dissimilatory sulfate-reducing bacteria that decompose fatty acids: III. Characterization of the filamentous gliding Desulfonema limicola gen. nov. sp. nov., and Desulfonema magnum sp. nov. *Arch. Microbiol.* 134 (4), 286–294. doi:10.1007/bf00407804

Wilkin, R. T., Barnes, H. L., and Brantley, S. L. (1996). The size distribution of framboidal pyrite in modern sediments: an indicator of redox conditions. *Geochem. Cosmochim. Acta.* 60 (20), 3897–3912. doi:10.1016/0016-7037(96)00209-8

Wilkin, R. T., and Barnes, H. L. (1996). Pyrite formation by reactions of iron monosulfides with dissolved inorganic and organic sulfur species. *Geochem. Cosmochim. Acta.* 60 (21), 4167–4179. doi:10.1016/s0016-7037(97)81466-4

Williams, K. H., Ntarlagiannis, D., Slater, L. D., Dohnalkova, A., Hubbard, S. S., and Banfield, J. F. (2005). Geophysical imaging of stimulated microbial biomineralization. *Environ. Sci. Technol.* 39 (19), 7592–7600. doi:10.1021/es0504035

Wolin, E. A., Wolin, M. J., and Wolfe, R. S. (1963). Formation of methane by bacterial extracts. *J. Biol. Chem.* 238 (8), 2882–2886.

Wolthers, M., Van der Gaast, S. J., and Rickard, D. (2003). The structure of disordered mackinawite. *Am. Mineral.* 88 (11-12), 2007–2015. doi:10.2138/am-2003-11-1245

Xiong, Y., Guilbaud, R., Peacock, C. L., Cox, R. P., Canfield, D. E., Krom, M. D., et al. (2019). Phosphorus cycling in Lake Cadagno, Switzerland: a low sulfate euxinic ocean analogue. *Geochem. Cosmochim. Acta.* 251, 116–135. doi:10.1016/j.gca.2019.02.011

Zeng, Y., Wang, H., Guo, C., Wan, J., Fan, C., Reinfelder, J. R., et al. (2018). Schwertmannite transformation via direct or indirect electron transfer by a sulfate reducing enrichment culture. *Environ. Pollut.* 242, 738–748. doi:10.1016/j.envpol.2018.07.024

Zhou, C., Vannela, R., Hayes, K. F., and Rittmann, B. E. (2014). Effect of growth conditions on microbial activity and iron-sulfide production by Desulfovibrio vulgaris. *J. Hazard Mater.* 272, 28–35. doi:10.1016/j.jhazmat.2014.02.046

Conflict of Interest: The authors declare that the research was conducted in the absence of any commercial or financial relationships that could be construed as a potential conflict of interest.